Carbon xxx (2018) xxx-xxx

Contents lists available at ScienceDirect

Carbon

journal homepage: www.elsevier.com

Observation of ferromagnetic ordering by fragmenting fluorine clusters in highly fluorinated graphene

Qian Feng[a, b, *], Yongping Zheng[a, b], Jiaxin Li[a, b], Liqin Jiang[a, b], Yuda Lin[a, b], Qingying Ye[a, b], Luzhuo Chen[a, b], Zhigao Huang[a, b, **]

[a] Fujian Provincial Key Laboratory of Quantum Manipulation and New Energy Materials, College of Physics and Energy, Fujian Normal University, Fuzhou 350117, China
[b] Fujian Provincial Collaborative Innovation Center for Optoelectronic Semiconductors and Efficient Devices, Xiamen 361005, China

ARTICLE INFO

Article history:
Received 4 December 2017
Received in revised form 15 February 2018
Accepted 26 February 2018
Available online xxx

ABSTRACT

To synthesize nonmetallic magnets containing exclusively *s*-p orbitals with high magnetic moments and magnetic ordering is a great challenge in physics and material science. In this study, we report increased localized spin magnetic moments and observation of ferromagnetic ordering by annealing of fluorographene. It is found that the magnetic properties is sensitive to fluorine (F) distribution. The samples annealed at ca. 400–450 °C exhibits an interesting ferromagnetic state, attributing to the fragmentizing of big F clusters into many small F domains after thermo defluorination. There are high-intensity magnetic moments in the annealed samples because of the enhanced edge effect of small F clusters, which contribute to the magnetic ordering in fluorographene for a shrunken average spacing between localized moments. The increasing structure defects after annealing can be as new centers of small F domains, and greatly stabilize magnetically ordered state.

1. Introduction

The graphitic materials which could exhibit an unusual s–p electron magnetism have received particular attention in physics and material science [1,2]. Developing effective approaches to synthesize such nonmetallic magnets with high magnetization and magnetic ordering is vital in potential application [1]. The defects such as vacancies [3,4], zigzag edges [5–7], and adatoms [8–25], which locally break the delocalized π bonding network of the bipartite graphene lattice, are considered to be good routes to induce magnetic moments. By demonstrating the splitting of vacancy-induced localized state, the direct evidence of π magnetism for the atomic defects in graphene was observed by scanning tunneling microscope (STM) [4]. However, the vacancy-induced spin density is limited because of loss of structural stability in graphene-based materials [23]. Recently, a signature of interaction-induced spin ordering along zigzag edges was identified in narrow graphene nanoribbons, raising hopes of combining charge and spin manipulation [5].

Doping of graphene by light elements is proved to be an efficient method for introducing a strong magnetism whilst modifying the graphene's electric and chemical properties [8–25]. In the case of nitrogen and sulfur doping, the substitution of carbon by the light elements can induce magnetic ordering into the graphene derivatives owing to substitutional atoms provide delocalized π electrons which occupying narrow bands at the Fermi level [9,10]. The electrons show a split resonance close to the Dirac point, and the direct coupling between the spin polarization which extends over several nanometers in hydrogenated graphene (HG) [11]. The ferromagnetic ordering for HG is widely verified due to the remnant bonding network accompanied by the formation of unpaired electrons [12–16]. Fluorographene have similar microstructure to HG, both of them are matrix-host of sp^2–sp^3 hybridization for adatom clustering and patterning formation [16–22]. As well as HG, the density functional theory (DFT) calculations shows that F adatoms on graphene lead to long-range spin polarization essentially localized in C sublattice opposite to that where the F atom is adsorbed [18,19]. Moreover, the F-vacancy in a fluorinated domain can lead to localized defect states in the band gap [20]. Depending on the sites of F addition or F-vacancy geometry, these structures may exhibit ferromagnetic/antiferromagnetic spin ordering, resulting a net localized magnetic moment of a given domain [20,21]. It is calculated that fluorographene system fulfills the Stoner criterion to yield a ferromagnetic ground state, and the long-range magnetic coupling between magnetic moments decays exponentially with the distance between magnetic moments [18]. Considering the modification of electronic structure, the overlap of the adjacent Wannier orbitals lead to a direct

* Corresponding author. Fujian Provincial Key Laboratory of Quantum Manipulation and New Energy Materials, College of Physics and Energy, Fujian Normal University, Fuzhou 350117, China.
** Corresponding author. Fujian Provincial Key Laboratory of Quantum Manipulation and New Energy Materials, College of Physics and Energy, Fujian Normal University, Fuzhou 350117, China.
Email addresses: fengqian@fjnu.edu.cn (Q. Feng); zghuang@fjnu.edu.cn (Z. Huang)

https://doi.org/10.1016/j.carbon.2018.02.097
0008-6223/

ferromagnetic exchange interaction that can compensate the kinetic Anderson's super-exchange in semi-fluorinated graphene [22].

However, experimentally, it is reported that only paramagnetism in fluorographene induced by point defects, interpreted that local magnetic moments are mainly arising from the edges of F clusters on graphitic structures [23]. Although the fluorination of reduced graphene oxide can obtain a higher localized spin magnetic moments because the existing structure defects help to hinder F clustering, the average spacing between magnetic moments is still too large to have magnetic interaction at liquid helium temperature [24]. A novelty way show that introducing OH groups can prevent F from migrating and suppress the formation of non-magnetic island in hydroxofluorographenes, which show room temperature antiferromagnetic ordering [25]. Thus, in order to detect magnetic ordering in the fluorographene samples, one effective route is to keep trying to decrease the F cluster sizes and avoid the tendency towards F clustering [18]. In this work, we demonstrated a simple and feasible way to minified the F cluster size and suppress fluorine aggregation by thermal annealing of highly fluorinated graphene. It is found that thermal defluorination greatly increases the localized spin density, attributing to the fragmentizing of large F clusters and the increase of edge effect by producing a lot of small F clusters. The maximum value of 2 K magnetization at 65 kOe for the annealed samples is high up to ca. 2.01 emu/g, ca. 17 times higher than that of fluorographene before annealing. Strikingly, we can observe experimental evidence of ferromagnetic states in the samples annealed at ca. 400–450 °C. It is inferred that the shrunk average spacing between localized spins causes magnetic ordering in fluorographene with a long-range spin polarization. The widely distributed structure defects after annealing play a great role to stabilize magnetically ordered state. The realization of such fluorographene material with strong magnetism is of both fundamental and technological importance.

2. Experimental

2.1. Sample preparation

Graphene oxide was synthesized by a modified Hummers' method, and then annealed in Ar at 650 °C for 1 h to obtain the reduced graphene oxide (RGO). To exclude the presence of impurities, the RGO sample was washed with hydrochloric acid seven times and then with alcohol 10 times. Thereafter, the fluorinated sample (FRGO) was prepared by heating the mixture of RGO and XeF_2 with a mass ratio of 1:12 in Teflon container at 180 °C for 30 h under Ar atmosphere. The FRGO powder was then separated into batches, and annealed at different temperature for 1 h under Ar atmosphere. After cooling quickly to room temperature, the annealed samples (FRGO-350, FRGO-400, FRGO-425, FRGO-450, and FRGO-500, numeric numbers denote the centigrade degree of annealing temperature) were obtained, and stored in nitrogen atmosphere.

2.2. Characterization techniques

The morphologies of the samples were detected by transmission electron microscope (TEM, Tecnai G2 F20) with the equipment operated at an accelerating voltage of 200 kV. The Raman spectra were tested using a LABRAM-HR micro-Raman system with a laser source of 532 nm. The X-ray photoelectron spectra (XPS) were tested on PHI5000 Versaprobe (ULVAC-PHI) by use of Al Ka radiation. The EPR spectra were taken with a Bruker EMX X-band EPR spectrometer with an ER 4119 HS cavity (9.837 GHz) at 278 K. The magnetic properties of the samples were measured using a SQUID magnetometer with a sensitivity of less than 10^{-8} emu (Quantum Design MPMS–XL). We performed inductively coupled plasma analysis (ICP, Jarrell–Ash JA-1100) to detect the magnetic impurity elements (such as Fe, Co, Ni, or Mn) of all the samples after magnetic test, and found that the magnetic impurity of all the samples are confirmed to be below 22 ppm (Supplementary material, Table S1), contributing to negligible magnetic signal. The pre-treatment of the sample before ICP test is described detailedly in the supplementary material.

2.3. Computational details

DFT calculations were performed through the Vienna Ab Initio Simulation Package (VASP). Perdew-Burke-Ernzerhof (PBE) formulation of the generalized gradient approximation (GGA) was adopted to treat electron exchange and correlation [26]. The energy cutoff was 500 eV. The convergence criterion for ionic relaxations between two consecutive steps is 10^{-4} eV. The structural optimization is finished when the residual forces are less than 0.01 eV/Å. A set of $5\times5\times1$ Monkhorst-Pack scheme k-mesh including the Γ point was used for the Brillouin Zone integrations. To compute the barrier energies of the functional groups diffusion, we employed climbing image nudged elastic band method as implemented in VASP with 5 image structures between the two neighbouring site [27].

3. Results and discussion

Fig. 1a and b illustrate the typical TEM images of FRGO and FRGO-400. Fig. 1a shows that FRGO is micrometer-sized rippled layer, like a crumpled thin paper. In Fig. 1b, the sample FRGO-400 maintains the two-dimensional flexible structure, but it has more wrinkles, which may attribute to the thermal fluctuations and expansion during the annealing process [28]. Compared to FRGO, changes in the Raman spectra of FRGO after annealing are shown in Fig. 1c. For

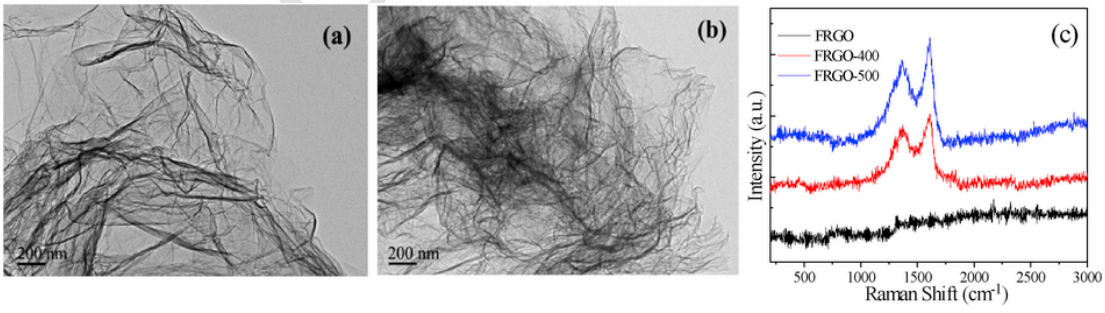

Fig. 1. Typical TEM images of (a) FRGO, (b) FRGO-400, and (c) Change in the Raman spectra before and after annealing. (A colour version of this figure can be viewed online.)

FRGO sample, it is seen that there is no discernible Raman signature in Raman spectra, which is similar with that of highly fluorinated graphene previously reported [29]. After annealing, the Raman data of the annealed samples show obvious G peaks (at ca. 1600 cm^{-1}), corresponding to graphene recovery. For FRGO-400, the appearance of characteristic disorder–induced peak (D peak) at ca. 1350 cm^{-1} with a high I_D/I_G (the ratio of the D peak to G peak) of 0.83, implies that it has high–concentration defects. For FRGO-500, although most of F adatoms were removed from the carbon skeleton (analyzed by the following XPS analysis), it still shows an I_D/I_G value of 0.79, indicating that thermal annealing obviously cause many significant structure defects when annealed at a high temperature.

Fig. 2a gives the survey XPS of the samples. FRGO displays two prominent peaks at 688.8 and 833.8 eV corresponding to photoemission of the F 1s core level and Auger electron [30,31]. It is seen that the F signals decrease obviously, along with the increasing C 1s signals at ca. 284.5 eV when the annealing temperature is increased. The atomic percents of the samples can be derived from the quantitative analysis of the XPS. Together with C atomic percents and the residual mass of the annealed samples, approximately, one can calculate the C loss after annealing. It is seen in Table 1 that the F/C atoms ratio is ca. 1.00 for FRGO, and obviously declined to ca. 0.04 when the annealed temperature rise to 500 °C. Clearly, thermal annealing can induce defluorination in FRGO, and one can adjust the fluorinated degree by varying annealing temperature. It is also seen the O/C atoms ratio of FRGO is ca. 0.04, and is nearly invariable in the annealed samples. Upon comparison with O 1s spectra of FRGO (Supplementary material, Fig. S1), the component of oxygen containing groups is assigned to very small numbers of ether and carboxyl groups, indicating that hydroxyls and carbonyls are easily replaced by fluorine [30].

Fig. 2b gives the typical C 1s XPS spectra of FRGO, FRGO-400, and FRGO-500, which were fine-scanned and deconvoluted into several components. The locations of C1s XPS peaks corresponding to different chemical groups are also given in Table S2 [30,31]. Compared to FRGO, the annealed samples show an obvious increase in the percent of sp^2 C-C bonds, as well as a decrease in the intensity of the CF_n peaks, manifesting the reformation of sp^2 bonds and an evident defluorination. The contents of chemical groups of the samples determined from the deconvolution of C 1s spectra are shown in Fig. 2c. Combined with the carbon loss of the annealed samples, the loss of CF_n bonds was calculated and shown in Table 1. For FRGO sample, although the F/C is ca.1.00, there is a 14.99% of C-C sp^2 bonds, which indicates a non-negligible formation of multiply fluorinated carbons (CF_2 bonds: 15.25%, terminal CF_3 bonds: 3.97%) located at graphitic structure defects and edges, as is shown in Fig. 5b. In the thermal annealing of FRGO, the rupture is not only C-F bonds, while at the lattice defects of the fluorographene, the C-C bond is much weaker in CF-CF_n (n=2, 3) structure and easier to be broken, especially for terminal CF-CF_3 bonds [31]. Hence, shown in Fig. 2c, the decline of CF_n (n=2, 3) curves corresponds to the breaking of the CF-CF_n (n=2, 3) bonds, leading to the generation of CF_n fragments. For FRGO-350, the number of CF_2 bonds is almost invariant, and the number of CF_3 bonds dropped by ca. 3%, shown in Table 1, which is in line with the carbon loss of ca. 3%. It is inferred the carbon loss of FRGO-350 primarily originates from the rupture of CF-CF_3 bonds. For FRGO-400, the drop of CF_n (n=2, 3) bonds is 9.51%, which is smaller than the carbon loss of 11.76%. That is, when the samples annealed at higher temperatures (≥400 °C), it is reasonably speculated that the loss of skelton C atoms is because of not only the preferable break of CF-CF_n (n=2, 3) bonds to CF_n fragments, but also the producing of some new C vacancies on the carbon networks. The F loss owes to not only the rupture of CF-CF_n (n=2, 3) bonds, but also the break of some C-F bonds. In addition, because C–CF corresponds to the sp^2 carbon atoms located near the CF groups, the average edge effect of F clusters can be characterized as $\psi = S_{C-CF}/S_{CF}$ [33]. S_{C-CF} and S_{CF} are the integral intensities of the components C—CF and CF, respectively. Seen in Fig. 2c, the ψ values of the samples increase

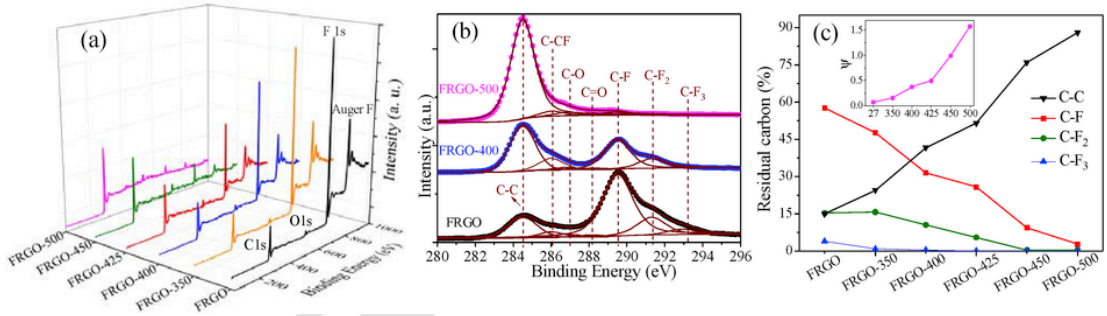

Fig. 2. (a) The survey XPS spectra of FRGO and the defluorinated samples annealed at different temperatures. (b) The typical C 1s XPS of the samples, which were fine-scanned and deconvoluted into several components. (c) The chemical compositions of the samples determined from the deconvolution of C 1s spectra. Inset is the dependence of ψ values on annealed temperatures. (A colour version of this figure can be viewed online.)

Table 1
The atomic percents of the samples derived from the quantitative analysis of the XPS, the residual mass $W_{residual}$, the loss of carbon and CF_n bonds of the samples after annealing.

	C	F/C	O/C	$W_{residual}$	C loss	CF loss	CF_2 loss	CF_3 loss
FRGO (%)	48.91	100.24	4.23	100	0	0	0	0
FRGO-350 (%)	53.67	82.31	4.00	88.28	3.11	11.54	0.07	3.09
FRGO-400 (%)	63.13	54.23	4.16	68.36	11.76	29.95	5.94	3.57
FRGO-425 (%)	71.03	36.28	4.50	55.80	18.96	36.82	10.81	3.97
FRGO-450 (%)	86.90	10.51	4.56	40.29	28.40	50.94	14.93	3.97
FRGO-500 (%)	92.26	3.63	4.65	30.45	42.56	56.15	15.05	3.97

with the increase of the annealing temperature, confirming the fragmentizing of large F clusters and the decreasing size of F clusters when FRGO was annealed at higher temperature.

Subsequently, we carried out the magnetic measurements for FRGO and the annealed samples. It is found that only linear diamagnetism is observed in all the samples at 300 K (Supplementary material, Fig. S2). In the following, all data have been corrected for the diamagnetic contribution by subtracting the corresponding linear diamagnetic background at room temperature. The dependence of 2 K mass magnetization M on applied magnetic field H is shown in Fig. 3a. It is found the $M(H)$ curves of FRGO, FRGO-350, FRGO-500 are well described by the Brillouin function [23,24].

$$M = M_S\left[\frac{2J+1}{2J}Coth\left(\frac{2J+1}{2J}x\right) - \frac{1}{2J}Coth\left(\frac{x}{2J}\right)\right] \quad (1)$$

in Equation (1), saturation magnetization $M_S = NgJ\mu_B$, $x = gJ\mu_B H/\left(k_B T\right)$, N is the number of spins, g is the g–factor (assuming g=2), k_B is the Boltzmann constant, and J is the angular momentum number, which is equal to S due to a neglectable orbital moments (l=0) for carbon materials [34]. The fitted value of J for the samples is 1, which is similar with that reported in partially fluorinated graphene because of the diradical motifs [25]. The M_s values are 0.12 emu/g, 0.55 emu/g, and 0.81 emu/g for FRGO, FRGO-350 and FRGO-500, respectively. Fig. 3b shows the dependence of susceptibility χ on temperature T when H=3 kOe for the three samples. Inset are the corresponding $1/\chi$–T curves, which fit the Curie law curves $\chi = NJ(J+1)g^2\mu_B^2/\left(3k_B T\right)$ well, corroborating purely Curie–like paramagnetic behavior.

As is shown in the inset of Fig. 3a, the 2 K initial magnetization of FRGO-400, FRGO-425, and FRGO-450 samples at 65 kOe are 1.49 emu/g, 2.01 emu/g, 1.12 emu/g, much higher than other samples. Interestingly, the M curves of the three annealed samples are not fitted with the above Equation (1). It indicates there may be some magnetically ordered states in the three samples with higher magnetization, and an extra internal 'molecular' field within the mean-field approximation should be considered in Brillouin function. In brief, all the annealed samples have a stronger magnetism than that of FRGO. Especially for FRGO-425, the 2 K magnetization at 65 kOe is ca. 17 times higher than that of FRGO and more than twice higher than the reported maximum value of fluorographene [24].

In order to confirm if the magnetically ordered state appears in FRGO-400, FRGO-425, and FRGO-450, the 2 K magnetic hysteresis loop $M(H)$ are given in Fig. 4a. The applied magnetic field firstly decreased from 65 kOe to −65 kOe, and then increased back to 65 kOe, according to the sweep rates in Table S3. Surprisingly, one can find the remnant magnetization (M_r) and non-zero coercive field (H_c) in the $M(H)$ curves of the three annealed samples (inset of Fig. 4a), showing a solid evidence of ferromagnetic ordering. The M_r and H_c are ca. 0.01 emu/g and 105 Oe for FRGO-400, ca. 0.02 emu/g and 123 Oe for FRGO-425, ca. 0.01emu/g and 85 Oe for FRGO-450, respectively. In addition, it is found that the $M(H)$ curves of the three annealed samples are not saturated even when the field is high up to 65 kOe, indicating the co-exiting paramagnetic behavior. For FRGO-400 and FRGO-450, the hysteresis loops at 2 K can be separated to paramagnetic and ferromagnetic components by using the Brillouin function with J=1 and assuming saturation character of the ferromagnetic part (Fig. S3, Supplementary material) [9,10,25]. For FRGO-400, the fit value of ferromagnetic M_s is ca. 0.27 emu/g, and the paramagnetic M_s is ca. 1.22 emu/g. For FRGO-450, the ferromagnetic M_s is ca. 0.25emu/g, and the paramagnetic M_s is 0.87 emu/g. The ferromagnetic signal of FRGO-400 is a little stronger than FRGO-450. However, for FRGO-425, the ferromagnetic and paramagnetic contributions are not easily separated by following the above mathematical procedures, indicating that it exhibits more complicated magnetic property.

To study the transition temperature below which magnetic ordering can be observed, the susceptibility $\chi(T)$ curves of the three samples were performed in the range of 2–300 K at 1 kOe, shown in Fig. 4b–d. In coincidence with the hysteresis loop of the samples, it is seen that the $\chi(T)$ curves primarily feature two components: paramagnetism and ferromagnetism. The paramagnetic term was fitted using the Curie function over the whole temperature interval, and two-component fit involving a combination of the Curie-Weiss law (i.e., $\chi_{ferro} = C'/(T - T_c)$) was used above the Weiss temperature T_c. By subtracting the paramagnetic signal with the derived parameter from $M(H)$ curves, the remaining χ' for both FRGO-400 and FRGO-450 show obvious ferromagnetic feather. The paramagnetic term of FRGO-425 was also fitted using the Curie law with J=1, and the fit value of the paramagnetic M_s is 1.42 emu/g. There is a hump in the remaining part χ' of FRGO-425, which indicates exactly complicated magnetic property including both ferromagnetic and relatively negligible antiferromagnetic features, similar with the previous studies [10,13]. From the fit of the remaining ferromagnetic part by the Curie-Weiss law, one

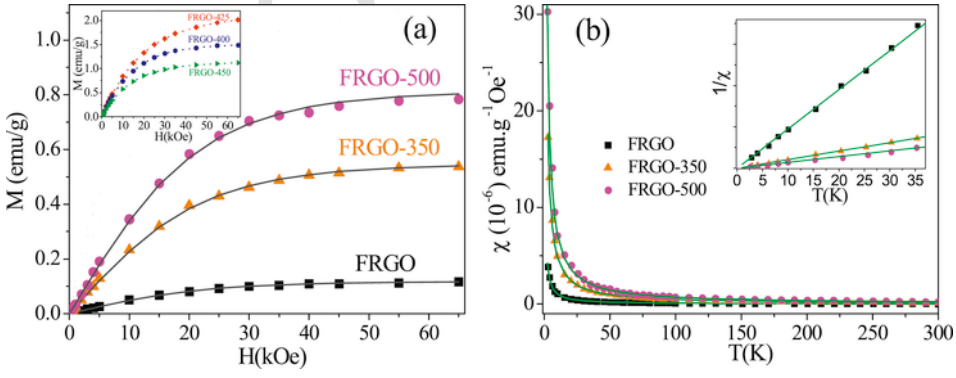

Fig. 3. (a) The initial magnetization curves $M(H)$ of FRGO, FRGO-350, FRGO-500 measured at 2 K. Symbols are measured data, and the solid curves are fitted curves of Brillouin function. Inset is the 2 K magnetization of FRGO-400, FRGO-425, and FRGO-450 samples. (b) Typical $\chi(T)$ curves of FRGO, FRGO-350, FRGO-500 under an applied field of 3 kOe. Inset is the corresponding $1/\chi(T)$, and the solid lines are fitted lines of the Curie law. (A colour version of this figure can be viewed online.)

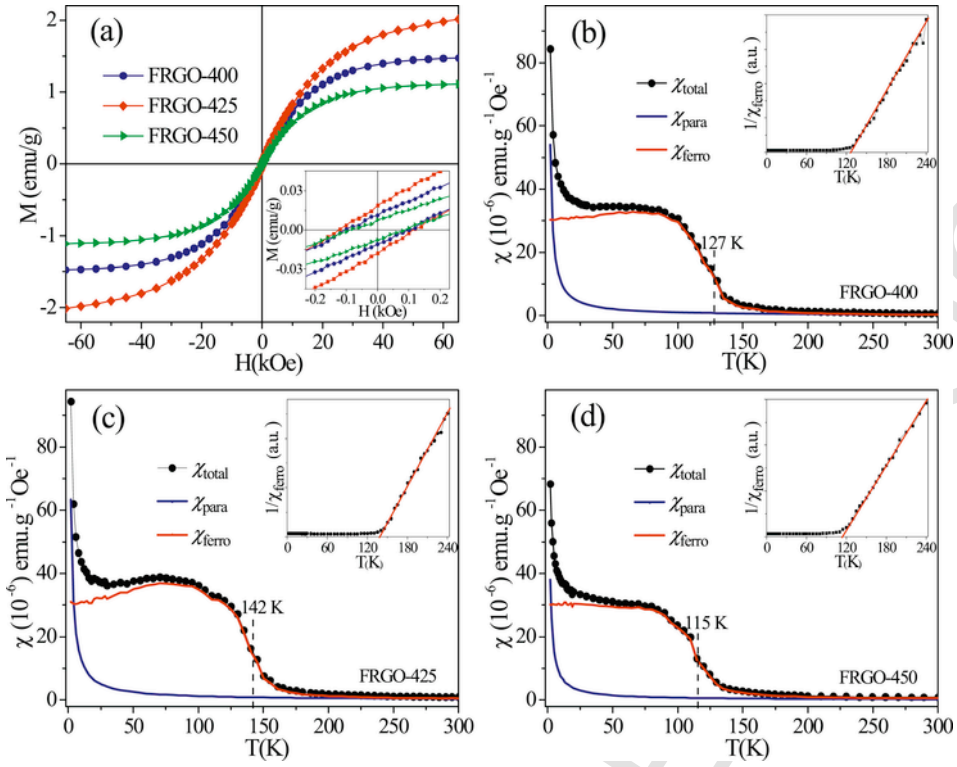

Fig. 4. (a) The 2 K magnetic hysteresis loop $M(H)$ for FRGO-400, FRGO-425, and FRGO-450. Inset is a part of the 2 K $M(H)$ curves. (b–d) The $\chi(T)$ curves of FRGO-400, FRGO-425, FRGO-450 under 1 kOe field, confirming the magnetic ordering of the three samples. The black curves are the measured data, and the blue are the fitting curves for paramagnetism by the Brillouin function. Red curves reflect the ferromagnetic magnetization by subtracting the paramagnetism from the measured curves. (A colour version of this figure can be viewed online.)

can derived the T_c values of 127 K for FRGO-400, 142 K for FRGO-425 and 115 K for FRGO-450, shown in the insets of Fig. 4b–d. Based on the above magnetic analysis, it is found that the enhancement of the magnetic response after the annealing process is mainly originating from the increasing of isolated paramagnetic centers, and the samples annealed at appropriate temperatures (ca. 400–450 °C) have increased intensity of magnetic moments, which are high enough to induce interaction between these magnetic moments. The sample with higher magnetic moments has a more obvious magnetic ordered signal and a higher T_c value.

To confirm the induced magnetism originating from local magnetic moments of dangling bonds experimentally, we measured the EPR spectra for the synthesized samples. Fig. S4 shows the typical EPR spectra of FRGO and the annealed samples. It is seen that the EPR signals of the samples with a characteristic g value of ~2.003, which have been identified in fluorinated carbon as free radicals and/or localized structural defects [25,35]. The unresolved hyperfine structure may due to different configurations of dangling bond centers and the surrounding neighbouring fluorine nuclei [35]. The inset gives a part of the magnified spectrum. It clearly shows the presence of triplet species, similar with that reported in Ref. 25 due to the diradical motifs of fluorographene. In particular, it is found in Fig. S4 that the EPR signal intensity increases after the thermal annealing. It is because that the defluorination leads to more residual sp^2-carbons with dangling bonds, indicating more paramagnetic centers. The EPR signal of FRGO-425 is much stronger than the other samples, which is similar to the evolution of M_s observed in $M(H)$ curves. At the same time, it is found that the peak-to-peak linewidth increases from 12 ± 1 (FRGO-350) to 30 ± 1 Oe (FRGO-425). The wider linewidth of FRGO-425 could be interpreted by the joint effect of dipole-dipole and exchange interactions between paramagnetic centers [36].

The electron paramagnetic resonance (EPR) is also a very sensitive local probe to detect magnetic impurities [37]. There is no characteristic hyperfine patterns of Mn^{2+} ions or other metal ions in the EPR of our samples (shown in Fig. S4), indicating that the samples are highly purified. Actually, the magnetic impurity elements (Fe, Co, Ni, or Mn) of all the samples were measured to be below 22 ppm by ICP test, and their contribution to the samples' magnetic response was estimated to be of the order of 10^{-8} emu $g^{-1}Oe^{-1}$ at 0 K under 1 kOe magnetic field [10]. It is several orders of magnitude lower than the measured mass magnetic susceptibility of our samples (10^{-5} emu $g^{-1}Oe^{-1}$), which can be almost neglectable.

Fig. 5 gives an intelligible model to better understand the magnetic properties of fluorographene after thermal annealing. In order to study the thermodynamic stability of F atoms on fluorographene, we first focus on the investigation of the binding energy E_b of the F-C bond at different surrounding based on the DFT computations. The corresponding structure is shown in Fig. 5a. Our calculated E_b of the F-C bond in fully fluorinated area is −5.01 eV, which is higher than the maximum value (−3.85 eV) of the F-C bond at different position of graphene/fluorographene interface [38]. Compared to the F adatoms inside the F clusters, the relatively lower stability of F atoms at the interfaces will induce a preferential evaporation or diffusion in the thermal annealing process. The E_b of the F-C bond near the vacancy (E_b of No. 1 position = −4.42 eV) is higher than that of isolated F atom on the graphene (−1.92 eV) [38], which indicate that the F atoms adsorbed at the vacancy are very stable. To further demonstrate the high chemical activity of vacancy, the diffusion energy barriers for the F atom from the nearest probable positions to the C atoms (No.1, No.2, No.3) at the

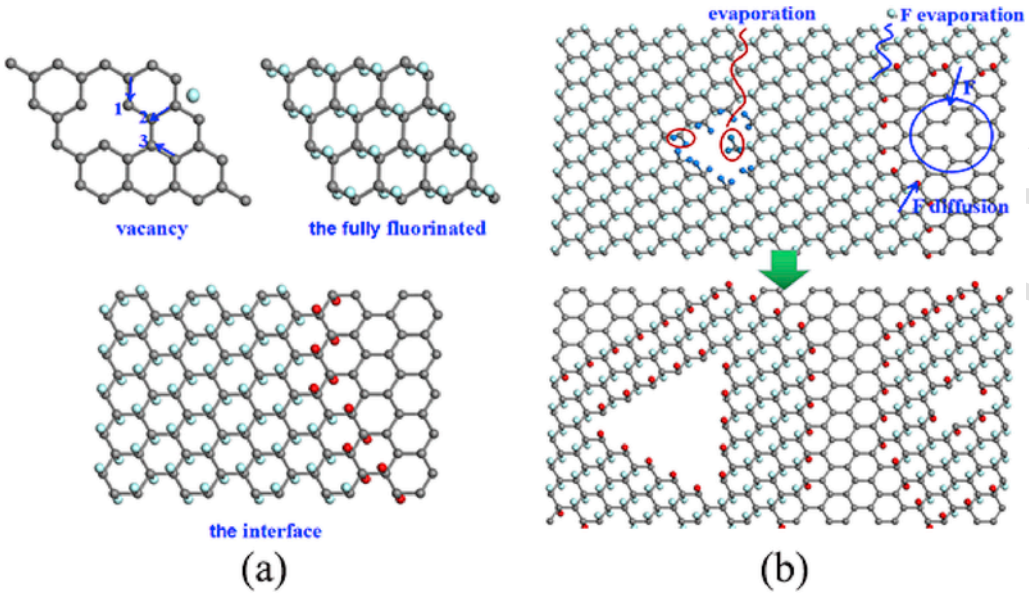

Fig. 5. (a) Atomic structure of fluorographene. The upper part is the supercell used in the calculations, and the lower part is atomic structure of graphene/fluorographene interface. (b) the schematic models of defluorination in the process of thermal annealing. The gray balls lattice represent carbon skeleton. A magnetic contribution is closely correlated with the edge adatoms of F clusters in —C—CF— structure (as indicated by red balls), while the magnetic contribution from the F adatoms in the interior of F cluster (as indicated by light blue balls), edge CF_n (n=2,3) (indigo balls) is expected to be zero [19,23]. (A colour version of this figure can be viewed online.)

vacancy are calculated, shown in Fig. S5. It is seen the three pathways to the three C atoms have low diffusion energy barriers, which are 0.18, 0.45, 0.14 eV, respectively. Therefore, vacancies are considered to be active sites and anchors for adatoms. F atoms preferably diffuse to vacancies and have a strong tendency towards clustering [17].

As shown in the upper part of Fig. 5b, for FRGO with a high fluorinated degree, the F clusters centered on carbon vacancies are relatively big, and the proportion of edge C—CF adatoms is low, resulting in a low magnetic moments with M_s value of 0.12 emu/g. When the samples is annealed at an appropriate temperatures (ca. 400–450 °C), combined with the above XPS analysis, the model is constructed as (shown in lower part of Fig. 5b): (i) the annealing prompt the producing of more new structure defects, which will be new centers of a number of small F clusters; (ii) compared to the adatom inside F cluster, F atoms at the interfaces will evaporate or diffuse preferentially, and the original large F clusters may convert to several small F domains with increased edge effect; (iii) the carbon vacancies of FRGO will evolve into larger structure defects because many multiply fluorinated carbons near vacancy defects makes FRGO readily attacked in thermal reduction [31]. As shown in Fig. 2c, the ψ of FRGO-425 is high to 0.497, corresponding to a large number of C—CF edge adatoms. It is in line with the constructed model of fragmentizing fluorine clusters in fluorographene by annealing. Compared to FRGO-425, even though the ψ value of FRGO-450 is higher, the number of edge adatoms decreases a little because of a decrease of F/C atoms ratio. In short, the samples annealed at moderate temperature can produce many small F-clusters, and they have lots of edge adatoms. Due to the bipartite nature of the graphene, the magnetic moment from the interior of an F cluster is expected to be zero. That is, magnetic contribution only comes from F cluster edges and is determined by a configuration of F adatoms near the edges. Only those F adatoms on the sublattice that have no counterparts on the neighbouring sites of the other sublattice will have magnetic contribution [23,24]. Moreover, different from the FRGO, the enlarging carbon vacancies are passivated by C-F bonds, which are calculated to have stable magnetic moments [39]. Thus, the intensity of magnetic moments is much enhanced, and the average spacing between magnetic moments located at the edges is expected to be greatly reduced because of the increasing intensity of localized spin magnetic moments.

Theoretically, the long-range magnetic coupling between localized spins is expected to take place for randomly distributed point defects and zigzag edges in graphene, and which falls off with the distance R between magnetic moments as 1/R [40]. In order to measure a ferromagnetic ordering in the F-graphene samples, it would be required to reduce the spacing between magnetic moments [18]. Hence, the samples annealed at ca. 400–450 °C which have quite high magnetic moments can exhibit obviously ferromagnetic states. Notably, the F adatoms at F-clusters' interfaces have higher diffusion energy barrier than that of an F atom on graphene [32,38], and thus the magnetic ordering induced along inward flanges of F clusters and interfaces of sp^2-conjugated islands embedded in an sp^3 matrix is stable [41]. For FRGO-350, the enhanced magnetism-inducing efficiency of F adatoms mainly come from the rupture of terminal CF_3 atoms. Thus, compared to the samples with magnetic ordering, FRGO-350 shows purely paramagnetic behavior with a lower intensity of localized magnetic moments. When FRGO was annealed at 500 °C, most of F adatoms were removed from the carbon skeleton. The magnetic contribution of FRGO-500 may derive from a sprinkling of F adatoms located at the vacancies, and the average spacing between two localized magnetic moments is too large to have magnetic interaction. On the whole, the magnetic properties of fluorographene present strong dependence on fluorine distribution. A shrunken spacing between two localized spins can lead to the magnetic ordering in the annealed FRGO samples. The widely distributed carbon vacancies can prevent migration of F atoms on the graphene derivative, and restrain the formation of non-magnetic F clusters, which stabilize magnetically ordered state.

4. Conclusions

In conclusion, we have annealed FRGO at different temperatures in Ar, and detected the enhanced localized spin magnetic moments. Such as FRGO-425, the magnetization at 65 kOe is high up to (2.01 emu/g), which is ca.17 times higher than that of FRGO. Interestingly, the samples annealed at ca. 400–450 °C exhibits an obvious magnetically ordered character. It must be attributed to the increasing number of carbon vacancies and the appropriate fluorine loss after thermal annealing, which conduce to the fragmentizing of large F clusters into many small fluorinated domains. The intensity of magnetic moments is thus greatly enhanced because of the increased edge effect of F clusters. It is found that the shrunken average spacing between two localized moments is clearly necessary for the magnetic ordering in fluorographene. Such annealed samples can undergo a transition from paramagnetic state to ferromagnetic ordered state by varying fluorinated degree and fluorine aggregation degree when annealed at different temperature. Our results will stimulate further investigations of magnetism and potential applications in adatom-engineered graphene.

Acknowledgements

This work was financially supported by the Natural Science Foundation of China (No. 11404059, No. 51773039, and No. 11504142) and the Natural Science Foundation of Fujian Province (Nos. 2016J01010, 2016J01291, 2017J01476, and 2017J01553).

Appendix A. Supplementary data

Supplementary data related to this article can be found at https://doi.org/10.1016/j.carbon.2018.02.097.

References

[1] O.V. Yazyev, Emergence of magnetism in graphene materials and nanostructures, Rep. Prog. Phys. 73 (2010), 056501.
[2] J. Cervenka, M.I. Katsnelson, C.F.J. Flipse, Room-temperature ferromagnetism in graphite driven by two-dimensional networks of point defects, Nat. Phys. 5 (2009) 840–844.
[3] J.J. Palacios, J. Fernández-Rossier, L. Brey, Vacancy-induced magnetism in graphene and graphene ribbons, Phys. Rev. B 77 (2008), 195428.
[4] Y. Zhang, S. Li, H. Huang, W. Li, J. Qiao, W. Wang, et al., Scanning tunneling microscopy of the π magnetism of a single carbon vacancy in graphene, Phys. Rev. Lett. 117 (2016), 166801.
[5] G.Z. Magda, X. Jin, I. Hagymasi, P. Vancso, Z. Osvath, P. Nemes-Incze, et al., Room-temperature magnetic order on zigzag edges of narrow graphene nanoribbons, Nature 514 (2014) 608–611.
[6] Z. Shi, I. Affleck, Effect of long-range interaction on graphene edge magnetism, Phys. Rev. B 95 (2017), 195420.
[7] P.P. Shinde, O. Groning, S. Wang, P. Ruffieux, C.A. Pignedolia, R. Fasela, et al., Stability of edge magnetism in functionalized zigzag graphene nanoribbons, Carbon 124 (2017) 123–132.
[8] E.J.G. Santos, A. Ayuela, D. Sanchez-Portal, Universal magnetic properties of sp^3-type defects in covalently functionalized graphene, N. J. Phys. 14 (2012), 043022.
[9] Y. Liu, N. Tang, X. Wan, Q. Feng, M. Li, Q. Xu, et al., Realization of ferromagnetic graphene oxide with high magnetization by doping graphene oxide with nitrogen, Sci. Rep. 3 (2013), 2566.
[10] J. Tucek, P. Blonski, Z. Sofer, P. Simek, M. Petr, M. Pumera, et al., Sulfur doping induces strong ferromagnetic ordering in graphene: effect of concentration and substitution mechanism, Adv. Mater. 28 (2016) 5045–5053.
[11] H. Gonzalez-Herrero, J.M. Gomez-Rodriguez, P. Mallet, M. Moaied, J.J. Palacios, C. Salgado, et al., Atomic-scale control of graphene magnetism by using hydrogen atoms, Science 352 (2016) 437–441.
[12] L. Xie, X. Wang, J. Lu, Z. Ni, Z. Luo, H. Mao, et al., Room temperature ferromagnetism in partially hydrogenated epitaxial graphene, Appl. Phys. Lett. 98 (2011), 193113.
[13] A.Y.S. Eng, H.L. Poh, F. Sanek, M. Marysko, S. Matejkova, Z. Sofer, et al., Searching for magnetism in hydrogenated graphene: using highly hydrogenated graphene prepared via Birch reduction of graphite oxides, ACS Nano 7 (2013) 5930–5939.
[14] E. Sasioglu, H. Hadipour, C. Friedrich, S. Blugel, I. Mertig, Strength of effective Coulomb interactions and origin of ferromagnetism in hydrogenated graphene, Phys. Rev. B 95 (2017), 060408.
[15] A.J.M. Giesbers, K. Uhlirova, M. Konecny, E.C. Peters, M. Burghard, J. Aarts, et al., Interface-induced room-temperature ferromagnetism in hydrogenated epitaxial graphene, Phys. Rev. Lett. 111 (2013), 166101.
[16] W.K. Lee, K.E. Whitener Jr., J.T. Robinson, P.E. Sheehan, Patterning magnetic regions in hydrogenated graphene via E-beam irradiation, Adv. Mater. 27 (2015) 1774–1778.
[17] H. Sahin, M. Topsakal, S. Ciraci, Structures of fluorinated graphene and their signatures, Phys. Rev. B 83 (2011), 115432.
[18] H.J. Kim, J.H. Cho, Fluorine-induced local magnetic moment in graphene: a hybrid DFT study, Phys. Rev. B 87 (2013), 174435.
[19] Y. Zheng, X. Wan, N. Tang, Q. Feng, F. Liu, Y. Du, Magnetic properties of double-side partially fluorinated graphene from first principles calculations, Carbon 89 (2015) 300–307.
[20] H.Y. Liu, Z.F. Hou, C.H. Hu, Y. Yang, Z.Z. Zhu, Electronic and magnetic properties of fluorinated graphene with different coverage of fluorine, J. Phys. Chem. C 116 (2012) 18193–18201.
[21] A. Nijamudheen, A. Datta, Pattern formation due to fluorination on graphene fragments: structures, hopping behavior, and magnetic properties, J. Phys. Chem. 117 (2013) 8506–8511.
[22] V.V. Mazurenko, A.N. Rudenko, S.A. Nikolaev, D.S. Medvedeva, A.I. Lichtenstein, M.I. Katsnelson, Role of direct exchange and Dzyaloshinskii-Moriya interactions in magnetic properties of graphene derivatives: C2F and C2H, Phys. Rev. B 94 (2016), 214411.
[23] R.R. Nair, M. Sepioni, I.L. Tsai, O. Lehtinen, J. Keinonen, A.V. Krasheninnikov, et al., Spin-half paramagnetism in graphene induced by point defects, Nat. Phys. 8 (2012) 199–202.
[24] Q. Feng, N. Tang, F. Liu, Q. Cao, W. Zheng, W. Ren, et al., Obtaining high localized spin magnetic moments by fluorination of reduced graphene oxide, ACS Nano 8 (2013) 6729–6734.
[25] J. Tucek, K. Hola, A.B. Bourlinos, P. Błonski, A. Bakandritsos, J. Ugolotti, et al., Room temperature organic magnets derived from sp^3 functionalized graphene, Nat. Commun. 8 (2017), 14525.
[26] J.P. Perdew, K. Burke, M. Ernzerhof, Generalized gradient approximation made simple, Phys. Rev. Lett. 77 (1996), 3865.
[27] H.J. Monkhorst, J.D. Pack, Special points for Brillouin-zone integrations, Phys. Rev. B 13 (1976), 5188.
[28] S. Deng, V. Berry, Wrinkled, rippled and crumpled graphene: an overview of formation mechanism, electronic properties, and applications, Mater. Today 19 (2016) 197–212.
[29] R.R. Nair, W.C. Ren, R. Jalil, I. Riaz, V.G. Kravets, L. Britnell, et al., Fluorographene: a two-dimensional counterpart of teflon, Small 6 (2010) 2877–2884.
[30] T. Chen, X. Wang, Y. Liu, B. Li, Z. Cheng, Z. Wang, et al., Effect of the oxygenic groups on the mechanism of fluorination of graphene oxide and its structure, Phys. Chem. Chem. Phys. 19 (2017) 5504–5512.
[31] W. Lai, D. Xu, X. Wang, Z. Wang, Y. Liu, X. Zhang, et al., Characterizations of the thermal/thermal oxidative stability of fluorinated graphene with various structures, Phys. Chem. Chem. Phys. 19 (2017) 19442–19451.
[32] L.G. Bulusheva, V.A. Tur, E.O. Fedorovskaya, I.P. Asanov, D. Pontiroli, M. Ricco, et al., Structure and supercapacitor performance of graphene materials obtained from brominated and fluorinated graphite, Carbon 78 (2014) 137–146.
[33] Y.V. Lavskayaa, L.G. Bulusheva, A.V. Okotrub, N.F. Yudanova, D.V. Vyalikh, A. Fonseca, Comparative study of fluorinated single- and few-wall carbon nanotubes by X-ray photoelectron and X-ray absorption spectroscopy, Carbon 47 (2009) 1629–1636.
[34] A.L. Kuzemsky, Unconventional and exotic magnetism in carbon-based structures and related materials, Int. J. Mod. Phys. B 27 (2013), 1330007.
[35] M. Dubois, K. Guerin, J.P. Pinheiro, Z. Fawal, F. Masin, A. Hamwi, NMR and EPR studies of room temperature highly fluorinated graphite heat-treated under fluorine atmosphere, Carbon 42 (2004) 1931–1940.

[36] M. Panich, A.I. Shames, T. Nakajima, On paramagnetism in fluorinated graphite: EPR and solid state NMR study, J Phys Chem Solds 62 (2001) 959–964.
[37] J. Vejpravova, B. Pacakova, M. Kalbac, Magnetic impurities in single-walled carbon nanotubes and graphene: a review, Analyst 141 (2016) 2639–2656.
[38] Z. Ao, Q. Jiang, S. Li, H. Liu, F.M. Peeters, S. Li, et al., Enhancement of the stability of fluorine atoms on defective graphene and at graphene/fluoro-graphene interface, ACS Appl. Mater. Interfaces 7 (2015) 19659–19665.
[39] N.K. Jaiswal, N. Tyagi, A. Kumar, P. Srivastava, Inducing half-metallicity with enhanced stability in zigzag graphene nanoribbons via fluorine passivation, Appl. Surf. Sci. 396 (2017) 471–479.
[40] M. Sherafati, S. Satpathy, RKKY interaction in graphene from the lattice Green's function, Phys. Rev. B 83 (2011), 165425.
[41] S. Okada, A. Oshiyama, Magnetic ordering in hexagonally bonded sheets with first-row elements, Phys. Rev. Lett. 87 (2001), 146803.